Eur. Phys. J. B **7**, 19–36 (1999)

THE EUROPEAN PHYSICAL JOURNAL B

EDP Sciences

Phase transitions of fluids confined in porous silicon: A differential calorimetry investigation

C. Faivre, D. Bellet[a], and G. Dolino

Laboratoire de Spectrométrie Physique[b], Université Joseph Fourier (Grenoble-I), B.P. 87, 38402 Saint Martin d'Hères Cedex, France

Received: 11 May 1998 / Revised and Accepted: 29 July 1998

Abstract. The phase transitions of non-polar organic fluids and of water, confined in the pores of porous silicon samples, were investigated by Differential Scanning Calorimetry (DSC). Two types of PS samples (p^- and p^+ type) with different pore size and morphology were used (with spherical pores with a radius of about 1.5 nm and cylindrical shape with a radius of about 4 nm respectively). The DSC results clearly show that the smaller the pores are, the larger is the decrease in the transition temperature. Moreover, a larger hysteresis between melting and freezing is observed for p^+ type than for p^- type samples. A critical review of the thermodynamical properties of small particles and confined fluids is presented and used to interpret and discuss our DSC results. The effects of the chemical dissolution as well as the influence of anodization time are presented, showing that thick p^+ type porous silicon layers are non-homogeneous. The DSC technique which was used for the first time to investigate fluids confined in porous silicon, enables us to deduce original information, such as the pore size distribution, the decrease in the freezing temperature of confined water, and the thickness of non-freezing liquid layer at the pore wall surface.

PACS. 81.65.-b Surface treatments – 64.70.Dv Solid-liquid transitions – 07.20.Fw Calorimetry

1 Introduction

Since the discovery of the visible photoluminescence of porous silicon (PS) by Canham [1] in 1990, many fundamental and applied researches have been performed on this material [2]. As the visible luminescence is usually related to quantum confinement effects in nanometer size silicon crystallites, it is important to have a good characterization of the shape and size of the silicon crystallites in PS [2,3]. Nevertheless, a systematic study of the correlation between luminescence energy and crystallites size (measured by Raman spectroscopy) was only published very recently by von Behren *et al.* [4]. In this paper we present new results on pore characterization based on the measurement of the decrease in the freezing or melting temperature of fluids confined in PS.

PS is obtained by an electrochemical etching in a hydrofluoric acid (HF) solution, of a single crystal silicon wafer. The main parameters controlling the porous structure are the type and the level of wafer doping, the HF concentration and the current density [5]. Porosity, an important structural parameter which can be easily measured by weighting, cannot describe completely a porous structure. Direct pictures of the PS structure were obtained by transmission electron microscopy [6]. For boron doped materials, two typical kinds of structures are observed: p^- type materials have a rather spherical pore structure, while p^+ type materials have a cylindrical structure with larger pore radii of a few nm. Electron microscopy can provide a direct image of the crystallite structure while other techniques recently reviewed by Hérino [7] give complementary information directly on the pore structure:

- the most usual method is based on capillary condensation of a vapor (usually N_2) inside the pores. From an estimation of the meniscus radius, given by the Kelvin relation, one can obtain a measurement of the pore radius. This method has been used by Hérino *et al.* [8] to determine pore size distribution in various kinds of PS samples: a radius of about 1.5 nm was found for p^- type whereas p^+ type have a pore radius in the 4 nm range;
- another method, developed by Brun *et al.* [9] and called thermoporometry, is based on the measurement of the decrease of the freezing temperature (ΔT) of a fluid confined in a porous structure. While ΔT can be easily measured by Differential Scanning Calorimetry (DSC), the interpretation of the experimental results is rather complex, and greatly depends on the pore geometry. The first results of this method applied on PS have been presented in a conference report [10].

The first aim of this paper is to apply thermoporometry to investigate the shape and size of pores in PS layers.

[a] e-mail: Daniel.BELLET@inpg.fr
[b] CNRS - UMR 5588

Moreover, the freezing of the fluid inside the PS layer is a useful process to freeze dry the sample [11] and, this study could be considered as a first step to understand better this drying method as well as the impregnation of complex fluids inside the pores to form nanocomposites with interesting optical properties for instance.

We first briefly recall the principles of thermoporometry with a critical review of the thermodynamics of small particles and confined materials. Then we give a description of some typical results on p^- and p^+ type PS samples, and we apply this method to study dissolution effects on pore size and water freezing in PS. We finally discuss some problems in the interpretation of thermoporometry (validity of thermodynamics relations, hysteresis phenomena, decrease of transition enthalpy, comparison with adsorption measurements) and we compare our results with previous measurements of PS structure.

2 Thermodynamics of small particle melting

It is well-known that, for small particles, the contribution of the surface energy to the thermodynamical behavior cannot be neglected. Shifts in the melting temperature and vaporization pressure proportional to the inverse of the particle radius are generally observed. This subject, which has been studied since the beginning of the century, has been clearly discussed in relation to surface equilibrium thermodynamics in the book of Defay and Prigogine, first published in french [12] in 1951 and, with some complements, in english [13] in 1966. Nevertheless, some aspects of the freezing of confined fluids are not described by equilibrium thermodynamics, and complex phenomena such as hysteresis remain under discussion. We first recall the main theoretical results of Defay and al. and the approximations used in their derivation. Then we consider the applications these results to the measurement of pore size, following mainly the work of Brun *et al.* [9,14] on thermoporometry.

2.1 Liquid-vapor transition of isolated droplets

Here we shall discuss only one component materials where three phases can be observed: solid (s), liquid (l) and vapor (v). Let us first consider a two phase system of a spherical liquid droplet coexisting in equilibrium with its vapor. The Gibbs-Duhem equations are satisfied in the two phases for small variations of the temperature T, of the pressure P_i and of the chemical potential μ_i of each phase i

$$s_i \delta T - v_i \delta P_i + \delta \mu_i = 0 \tag{1}$$

where s_i and v_i are the molar entropy and volume of phase i. The system must also be in mechanical equilibrium: the pressure P_l of a liquid droplet of radius r_l in equilibrium with its vapor at pressure P_v, verifies the Laplace equation: $P_l - P_v = 2\gamma_{lv}/r_1$, where γ_{lv} is the surface energy of the droplet.

Neglecting v_l relative to v_v and assuming a perfect gas approximation for the vapor in Gibbs-Duhem and Laplace equations, and varying pressure at a constant temperature, one arrives to the Kelvin equation (W. Thomson (Lord Kelvin)) [15], that gives the pressure P_v of a vapor in equilibrium with a liquid droplet of radius r_l:

$$\mathrm{Ln}\frac{P_v}{P_0} = \frac{2\gamma_{lv}}{r_1}\frac{v_1}{RT} \tag{2}$$

where P_0 is the pressure of the vapor in equilibrium with the bulk liquid at a temperature T.

In a similar way, for the variation of temperature at constant vapor pressure, one can obtain the relation [13]

$$\mathrm{Ln}\frac{T^*}{T_0} = -\frac{2\gamma_{lv}}{r_1}\frac{v_1}{\Delta H_{lv}} \tag{3}$$

where ΔH_{lv} is the transition enthalpy, T_0 is the bulk transition temperature and T^* is the temperature of equilibrium between a liquid droplet and its vapor. Note that T^* is often identified with the vaporization temperature.

Equations (2, 3) are directly related to the modification of the chemical potential induced by the existence of a surface curvature, which is known as the Gibbs-Thomson effect.

2.2 Application to phase transitions of isolated crystals

2.2.1 Two phases

The conditions for the extension of the discussed thermodynamic approach to small crystals with anisotropic equilibrium shapes have been discussed by Defay *et al.* [13]. In a first approximation a small crystal is equivalent to a spherical particle of radius r_s with an average isotropic surface energy γ_{sl}. Thus for a two phase system (solid-liquid), one obtains an equation similar to equation (3)

$$\frac{\Delta T}{T_0} = -\frac{2\gamma_{sl}}{r_s}\frac{v_s}{\Delta H_{sl}} \tag{4}$$

where for small $\Delta T = T^* - T_0$, the $\mathrm{Ln}(T^*/T_0)$ term has been replaced by $\Delta T/T_0$. In fact, at the temperature T^*, a crystallite of radius r_s is in unstable equilibrium with its melt. In modern literature, equation (4) is known as Gibbs-Thomson equation by analogy with equation (3). This is somewhat ambiguous since the possibility of a variation of the melting temperature for a solid particle was first mentioned (without formula) by J.J. Thomson in 1888 [16]. According to Kubelka [17], equation (4) for a solid-melt equilibrium, was published by Rie [18] around 1920.

2.2.2 Three phases

However, due to the possible presence of vapor phase during the melting of a solid, the equilibrium of three

phases [13] has often to be considered. For bulk materials, the equilibrium between three phases occurs only at the triple point, for unique values of T and P. However for small objects, the curvatures of two interfaces act as supplementary thermodynamic variables. Thus, depending on the curvature of these two interfaces, an equilibrium state can be found for various values of P and T. Following Defay *et al.* [13], one can derive various equations determined by the morphology of the three phase interfaces. Actually the two principal cases reported in the literature correspond to the presence of only two menisci.

Isolated spherical crystal and liquid droplet in their vapor

This case was considered by Pawlow [19] in 1909, without giving the explicit variation of ΔT. Here also one starts with the Gibbs-Duhem equations of the three phases. Using Laplace equation and neglecting v_s and v_l relative to v_v, the shift of the melting temperature ΔT of a solid sphere of radius r_s in equilibrium with a liquid sphere of radius r_l, both in contact with their common vapor, is

$$\frac{\Delta T}{T_0} = -\frac{2}{\Delta H_{sl}}\left(\frac{v_s\gamma_{sv}}{r_s} - \frac{v_1\gamma_{lv}}{r_l}\right). \quad (5)$$

If a solid sphere and a liquid droplet have equal mass, the number of parameters can be reduced. Using the densities ρ_s and ρ_l, Hanszen [20] obtained a relation often used for the melting of spherical metallic particles:

$$\frac{\Delta T}{T_0} = -\frac{2}{r_s\rho_s\Delta H_{sl}}\left[\gamma_{sv} - \gamma_{lv}\left(\frac{\rho_s}{\rho_l}\right)^{2/3}\right]. \quad (6)$$

This is, in fact, the equation for the triple point equilibrium of a small particle. As discussed in Section 5.1, equations (4, 6) are equivalent if one neglects the change of density and if one accepts the validity of the relation

$$\gamma_{sv} - \gamma_{lv} = \gamma_{sl}. \quad (7)$$

Spherical crystal inside a liquid shell surrounded by its vapor

This case was introduced by Reiss and Wilson [21]. With some reasonable approximations, Gibbs-Duhem equations lead to the liquid shell equation (8)

$$\frac{\Delta T}{T_0} = -\frac{2}{\Delta H_{sl}}\left(\frac{v_s\gamma_{sl}}{r_l - t_0} - \frac{(v_1 - v_s)\gamma_{lv}}{r_l}\right). \quad (8)$$

In this form, given by Hanszen [20], the liquid shell of external radius r_l has an undetermined thickness t_0 which is often used as a fitting parameter. If one neglects t_0 and the term $(v_l - v_s)$, which corresponds to the effect of the pressure of the liquid shell on the crystalline core given by Clapeyron relation, equation (8) is again equivalent to the Gibbs-Thomson equation (4).

If three phases are present, separated by three menisci, one meniscus radius is a function of the two others, and the various three phase equations are not independent [9].

2.3 Thermodynamic equilibrium melting temperature

Equations (4–6, 8) give a melting temperature T^*, which corresponds to an unstable equilibrium between the solid and the liquid phases. It is also useful to consider other definitions of the melting temperature. It was only in 1975 that Peppiat and Sambles [22] introduced the temperature T_e at which a small particle has the same free energy in the solid and in the liquid phases. With F_i the bulk free energy of phase i and $r_s = r_l = r$, one gets for a spherical particle

$$\Delta F = \frac{4}{3}\pi r^3 F_s + 4\pi r^2\gamma_{sv} - \left(\frac{4}{3}\pi r^3 F_l + 4\pi r^2\gamma_{lv}\right). \quad (9)$$

At the thermodynamic equilibrium, $\Delta F = 0$. With:

$$F_s - F_l = \frac{\Delta H_{sl}}{v_s}\frac{(T_e - T_0)}{T_0},$$

one gets

$$\frac{\Delta T}{T_0} = \frac{T_e - T_0}{T_0} = -3\frac{(\gamma_{sv} - \gamma_{lv})v_s}{r\Delta H_{sl}}\,. \quad (10)$$

Using equation (7), this relation becomes

$$\frac{\Delta T}{T_0} = -\frac{3\gamma_{sl}}{r_s}\frac{v_s}{\Delta H_{sl}}\,. \quad (11)$$

This equation, defining the thermodynamic equilibrium melting temperature T_e, is similar to the Gibbs-Thomson equation (4), but now with a numerical coefficient 3, instead of 2.

Similar calculations can be performed for a cylinder of radius r and length L (neglecting the energies of the two ends) [23],

$$\Delta F = \pi r^2 L F_s + 2\pi L r\gamma_{sv} - (\pi r^2 L F_1 + 2\pi r L\gamma_{lv}). \quad (12)$$

Here also, two melting temperatures can be defined, the thermodynamic equilibrium T_e where $\Delta F = 0$, with the coefficient 2 in equation (11), and the interface equilibrium T^*, with a coefficient 1. For spherical and cylindrical shapes, T^* corresponds to the unstable equilibrium of the solid-liquid interface, occurring for the maximum value of ΔF, given by $d(\Delta F)/dr = 0$. Similar results were also obtained by Couchman *et al.* [24] who further associated them with nucleation phenomena. The fact that melting no longer occurs at a well defined temperature can be related to the existence of a thermal hysteresis as suggested by Couchman *et al.* [24].

2.4 Phase transition of confined materials

It is well-known that the phase transitions of materials confined in small pores are also influenced by the effects of curvature, as shown by two typical situations:

– capillary condensation of a liquid phase in a porous solid occurs at a vapor pressure lower than the saturation pressure of the bulk liquid, and the meniscus radius is related to the vapor pressure through the Kelvin equation [13];

– melting of a confined material occurs generally at a temperature lower than that of bulk melting. As for isolated crystals, Defay *et al.* [13] have shown that various cases must be considered according to the topology of the various interfaces. We consider the ideal case of a liquid in a circular cylinder of radius r with a solid-liquid interface. Then all the interfaces are spherical with radii R_{sl}, related to r by $r = R_{sl}\cos\theta_{lw}$, where θ_{lw} is the contact angle of the liquid with the wall (w) given by Young equation:

$$\gamma_{sl}\cos\theta = \gamma_{sw} - \gamma_{lw}. \tag{13}$$

For complete wetting ($\theta_{lw} = 0$), equation (13) is similar to equation (7). For a fluid confined in a cylindrical pore, in the case of perfect wetting ($\theta_{lw} = 0$), one again obtains the Gibbs-Thomson equation (4). Brun *et al.* [9,14] proposed that the lowering of the transition temperature of a confined fluid can be used to determine the pore diameter. The classical thermodynamic approach of Defay *et al.* [13] describes the solid-liquid interfaces at equilibrium but such interfaces need first to be created. Therefore, several mechanisms have been considered.

(i) *Nucleation*
It is a probabilistic effect according to the classical nucleation theory [25]. Applied respectively to crystallization and to melting, this theory gives a shift of the transition temperature below and above the equilibrium transition temperature of the confined fluid, leading to a thermal hysteresis. When the pore wall is wetted by the fluid, nucleation occurs inside the liquid with a large undercooling. Scherer [26], in a critical discussion of freeze drying and thermoporometry, states that for freezing, nucleations in pores are rare events. On the other hand, if the solid wets the pore walls, crystal nucleation is easier and occurs on the pore wall.

(ii) *Penetration of a solid front*
A layer of bulk liquid is often present outside the porous material in experiments of confinement in porous solids. During cooling the bulk liquid freezes first, giving a solid crust on the external surface, while the fluid inside the pores remains liquid. Freezing in the pores occurs at the temperature T^* given by Gibbs-Thomson equation (4) [27], when the spherical meniscus between external solid and the internal liquid enters inside the pores. It is clear that such a phenomenon can exist only in cooling and that melting should come from another nucleation phenomenon. This can be at the origin of a thermal hysteresis.

(iii) *Outgoing of the fluid from the pores*
In the presence of a temperature gradient, the liquid inside the pores can evaporate and freeze as a bulk crystal outside the pores [9,26]. For water in a soil, this slow phenomenon is at the origin of frost heaving [27,28]. It seems that these effects are not really important in DSC measurements. In the following, we consider that freezing occurs through the penetration of an external solid front while melting occurs due to the instability of a melt-solid interface.

For the quantitative interpretation, two other phenomena, often observed in phase transitions of confined materials, have to be taken into account:

– hysteresis is a frequent effect which can be related to mechanisms (i) or (ii). It is clear that nucleation always produces a thermal hysteresis. Another explanation of hysteresis in cylindrical pores, proposed by Brun *et al.* [9,14], is related to a difference in interface shapes between freezing and melting. Upon cooling, freezing occurs through the penetration of a solid front, that has a spherical interface of radius r (equal to the pore radius if the contact angle $\theta = 0$). Then the shift of the transition temperature, ΔT, is given by $\Delta T/T_0 = -2\gamma_{sl}v_s/r\Delta H_{sl}$ according to the usual Gibbs-Thomson equation. In the case of heating, Brun *et al.* [9,14] proposed that the nucleation of the cylindrical fluid shell occurs first on the pore walls, with a curvature $1/r$. In this case, the shift in the temperature ΔT, given by $\Delta T/T_0 = -\gamma_{sl}v_s/r\Delta H_{sl}$, is only a half of that for cooling. We will use this fact for the interpretation of the experimental results, leaving the discussion to Section 5;
– non-freezing layers are often observed in the vicinity of the interface between a confined fluid and the matrix, especially in the case of water, and produce an apparent decrease of the transition enthalpy [29]. Upon heating, these non-freezing layers favor the nucleation of the liquid shell mentioned above for the hysteresis mechanisms.

2.5 Conclusion

As we have seen, with two approximations (neglect of the volume difference between liquid and solid phases and the use of Eq. (7)), one obtains the Gibbs-Thomson equation for the shift in the transition temperature. To interpret our measurements, we use the general form of equation (11)

$$\frac{\Delta T}{T} = -\alpha\frac{\gamma_{sl}}{r}\frac{v_s}{\Delta H_{sl}}\cdot \tag{14}$$

The coefficient α depends on the experimental conditions as shown in Table 1: for a spherical shape, $\alpha = 2$ for the unstable meniscus equilibrium at T^* and $\alpha = 3$ for the thermodynamical equilibrium at T_e. For a cylindrical shape, the corresponding values are $\alpha = 1$ and $\alpha = 2$. In the rest of the paper, we will use the results presented here to interpret the measurements performed on PS.

3 Experimental conditions

3.1 Porous silicon formation

The PS layers were obtained by anodization of boron-doped (001) silicon wafers. Both highly doped (p^+ type) silicon wafers of 10^{-2} Ωcm resistivity and lightly doped

Table 1. Dependence of the α coefficient value of equation (14), on the pore geometry for the various kinds of thermodynamic phenomenon considered for the phase transition (see Sect. 2). For the interpretation of our results, only the cases corresponding to the lower two lines, are considered.

	Transition	Spherical pores	Cylindrical pores
Thermodynamic equilibrium	melting and freezing	$\alpha = 3$	$\alpha = 2$
Stability limit of the liquid layer at the pore wall interface	melting	$\alpha = 2$	$\alpha = 1$
Unstable equilibrium of a spherical solid-liquid meniscus	freezing	$\alpha = 2$	$\alpha = 2$

Table 2. Electrochemical formation conditions of p^- and p^+ type PS samples (j is the current density).

type	porosity (%)	[HF] (%)	[water] (%)	[ethanol] (%)	j (mA/cm^2)	time (s)	thickness (μm)
p^-	65	35	35	30	50	1120	50
p^+	60	25	25	50	180	700	100

Table 3. Physical properties of the different fluids used in the DSC experiments. The γ_{sl} values, in italic, correspond to values calculated as explained in the text. The value of γ_{sl} for cyclohexane is from reference [32].

Liquid		Transition temperature (K)	Latent heat of transition: ΔH_{sl} (J/g)	Interfacial free energy γ_{sl} (mJ/m^2)
cyclo-hexane	$s-l$	279.5	31.9	4.6
	$s-s$	186	79.8	*9*
dodecane		263	214	*13.5*
water		273	334	*25–26*

(p^- type) Si wafers of 4–6 Ωcm resistivity were investigated. The formation conditions of the porous layers are presented in Table 2.

To detach the porous layer from the silicon substrate, an electrolyte with lower HF concentration (5% HF, 45% water and 50% ethanol) was used and a higher current density (500 mA/cm^2) was applied for 5 to 10 s to reach the electropolishing conditions. As it was sometimes difficult to perform this experiment on layer thinner than 50 μm, we only present results on porous layers with a thickness larger than 50 μm.

A further chemical dissolution for some samples of both types, was performed by leaving the PS layers in the 5% HF solution, under dark conditions, for time varying from zero to 100 min (in an open circuit).

Some samples were thermally oxidized at 300 °C under oxygen atmosphere for 60 min to get a hydrophilic internal PS surface [30].

During this study it appeared that sample reproducibility, especially concerning p^+ type PS layers of 100 μm thickness, was not always satisfactory. For this reason, all the DSC curves presented on the same figure were obtained on the same day, on substrates coming from the same wafer.

3.2 Differential scanning calorimetry measurements

All the measurements were performed on a standard DSC apparatus (Perkin Elmer DSC2). The PS layers were filled with various organic liquids (alkane which perfectly wets the PS layer as observed in a previous X-ray experiment [31], or water with the oxidized samples). Some physical properties of these liquids can be found in Table 3.

Two different alkanes were used:

– cyclohexane (C_6H_{12}) exhibits two phase transitions: a solid-liquid transition and a solid-solid transition (monoclinic to cubic phase), and it has already been studied in DSC experiments on confined fluids [32,33];
– dodecane ($C_{12}H_{26}$) has a large latent heat of fusion, which gives a strong DSC signal for the phase transition of the confined liquid.

The values of surface energy (γ_{sl}) were estimated for dodecane, water and solid-solid transition of cyclohexane in relation to the cyclohexane solid-liquid interfacial energy value [32] of 4.6 mJ/m^2 in a reference measurement: a porous sample was separated in two parts, one was filled by cyclohexane and the second one by another liquid. One can assume that the pore radii calculated from solid-liquid cyclohexane phase transitions, is the same as the pore radii

Table 4. DSC values of the transition temperature shifts (ΔT) and of the Full Width at Half Maximum (FWHM) of the confined transition peak of dodecane confined in p^- and p^+ type PS layers, is measured. The pore radius (r) of the PS samples is calculated from the DSC results as described in Section 4.1.

sample	transition	α in Eq. (14)	ΔT (K)	FWHM (K)	r (nm)
p^+ 60%	freezing	2	20	7	2.1
			16.1		2.6
	melting	1	7.8	9.5	2.7
p^- 65%	freezing	2	32.4	7	1.3
	melting	2	28.4	7	1.5

estimated from the second liquid confined peaks. This unknown value of γ_{sl} is then estimated from the one of cyclohexane.

Each self-supported PS layer, of approximately 0.9 cm^2 surface, was introduced in an aluminum capsule after being broken in small pieces of a few mm^2. The resulting PS mass was between 1 and 2 mg and a few mg of liquid was introduced in the sample compartment, before hermetically enclosing the capsule.

The scanning temperature rates used were 10, 5 or 2.5 K/min, which were slow enough to avoid temperature gradient problems since the Full Width at Half Maximum (FWHM) of the confined DSC peaks remained nearly the same for the different scanning rates.

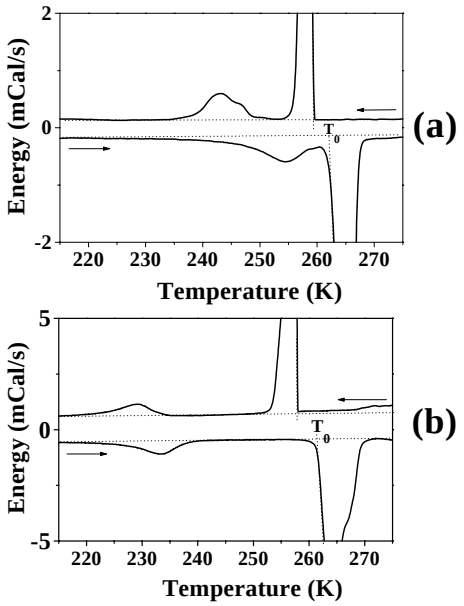

Fig. 1. DSC scans for decreasing and increasing temperature (as indicated by the arrows) at a scanning rate of 10 K/min, of the solid-liquid transition of dodecane confined in (a) a p^+ type PS sample of 60% porosity and 100 μm thickness, (b) a p^- type PS sample of 65% porosity and 50 μm thickness.

4 Experimental results

Firstly, in Section 4.1, we present some typical experimental DSC measurements related to p^- and p^+ type PS layers. Section 4.2 deals with pore size distributions of p^+ type samples as a function of anodization time and the effect of the chemical dissolution in HF on both types of samples. In Section 4.3, the investigation of water freezing in oxidized PS layers is reported. Finally, in Section 4.4, the latent heat of transition of confined fluid is estimated.

4.1 Comparison between p^+ and p^- type samples

4.1.1 p^+ type PS samples

Figure 1a exhibits a typical DSC curve which presents the freezing and melting scans of dodecane with a p^+ type PS sample of 60% porosity and of 100 μm thickness. The energy supplied to the sample is plotted *versus* the temperature which varies at a constant rate. The alkane confined in the nanometer-size pores of porous silicon, gives rise to a broad peak shifted down, while the rest of the liquid, outside the porous layer, behaves as a bulk liquid and thus gives an intense narrow peak at the bulk transition temperature.

For a bulk isothermal transition, the tangent to the peak represents the beginning of the transition process and determines the transition temperature. In Figure 1a, a thermal hysteresis of about 3 K is clearly observed for this bulk peak. This usual hysteresis is due to the small delay for the heterogeneous freezing nucleation of a pure liquid. On the other hand upon heating, nucleation occurs easily at the crystal surface. Then the bulk melting temperature is identified with the true equilibrium transition temperature and is taken as the reference bulk transition temperature T_0 in this work. The bulk peak FWHM is small and is only due to kinetic effects.

The peak corresponding to the confined fluid is broader but less intense than the bulk one. The DSC peak intensity depends on the latent heat of the fluid, the scanning rate and the amount of liquid involved in the transition. From the DSC freezing curve, the transition peak of the confined dodecane exhibits a FWHM of 7 K (see Tab. 4).

As the confined peak width is independent of the scanning rate, it is assumed that the peak width is related to the pore size distribution and that the maximum of the peak defines the average pore size. The values of temperature shifts for both transitions are reported in Table 4. A hysteresis of about 11 K is observed for the confined peak. The physical cause of such feature is certainly

different from that of the bulk hysteresis, since the transition mechanisms of a fluid confined in nanometric pores are different from those of bulk liquid as discussed in Section 2.

(i) *Freezing*
As the temperature decreases, the liquid outside the porous layer freezes first, at a temperature that is slightly below the equilibrium bulk freezing temperature. The freezing in the nanometric pores occurs through the slow penetration of a freezing front, with a spherical shape solid-liquid meniscus formed at the pore aperture. The penetration of this freezing front will be delayed in the smallest pore apertures, broadening the confined transition peak. Thus the FWHM of the freezing confined peak will depend on the size distribution of pore aperture in the porous layer.
The freezing transition occurs for spherical interface equilibrium conditions and depends on the meniscus shape only, which according to Scherer [26] is always spherical (for cylindrical pores as well as for spherical ones). The temperature shift when compared to the bulk is then given by equation (14) with $\alpha = 2$.

(ii) *Melting*
In principle, at low temperature, all the fluid inside and outside the pores is frozen. To melt, the organic solid has to nucleate a liquid layer of a few angstrom thick, and this is initiated at the pore wall surface. Then the melting of a confined material occurs at a temperature that lies between the equilibrium temperature and the temperature corresponding to the stability limit of the surface liquid layer [24,34]. Often, the transition of the confined material occurs at a temperature close to this stability limit and we assume that the measured temperature is equal to this last temperature. In this case, the relation between the melting temperature and the pore radius can depend on the pore geometry (spherical or cylindrical), and in equation (14) the coefficient value is $\alpha = 2$ for spherical pore and $\alpha = 1$ for cylindrical pore shape. For a cylinder, such variation in this coefficient [9,14] ($\alpha = 2$ for freezing and $\alpha = 1$ for melting), induced by a geometric effect, can explain the large hysteresis of the p^+ type PS samples that have a cylindrical pore morphology.

Relying on these main assumptions and, at first, neglecting the correction due to a possible non-freezing surface layer, one can evaluate a pore radius for the various samples studied, by deducing it from the melting and freezing DSC curves. Eventually, if these assumptions are valid, we shall find the same radius value either from melting or freezing curve.

It is also worth noting that in our case, the porous layer is electrochemically detached from the substrate, the top and the bottom of the layer may be slightly different. Therefore such an asymmetry can have on influence on front penetration. But Thönissen *et al.* [35] observed no influence of this separation process on PS morphology.

To calculate the pore radius from ΔT measurements, one has to know the value of γ_{sl} for dodecane. We estimated it from the value of γ_{sl} for cyclohexane as explained in Section 3.2, and we found $\gamma_{sl} = 13.5$ mJ/m^2, whereas a value of $\gamma_{sl} = 12.1$ mJ/m^2 has been reported [36].

Figure 1a exhibits a double peak shape for the confined freezing transition. From the temperature depression observed from these two peaks, two pore radii are found from equation (14) with $\alpha = 2$: $r = 2.1$ and 2.6 nm. The average pore radius, deduced from the melting curve (with $\alpha = 1$), is around 2.7 nm, rather close to the two values found on cooling. This can be considered as a justification for our analysis.

The FWHM of the melting confined peak is estimated around 9.5 K, whereas a FWHM of 7 K is observed for the freezing curve. The peak width is larger for heating which agrees with the fact that in this case the transition is really "sensitive" to all pore sizes. The measured values of ΔT and FWHM as well as the calculated pore radius values are reported in Table 4. We note that one indeed measures a smaller pore radius for freezing than for melting which is in agreement with the hypothesis of pore aperture limitation of the freezing front penetration. Moreover, the main feature of the p^+ type PS sample of 60% porosity and 100 μm thickness is its pore size distribution with two maxima. In the case of isotherm adsorption measurements, a broadening of the pore size distribution width was observed when increasing the current density and keeping the same electrolyte [8] to form p^+ type PS sample. In our case, the forming current density is rather high ($j = 180$ mA/cm^2), and this can explain a large pore size distribution. Nevertheless, a double pore size structure has not been reported for such a sample (to the authors' knowledge), but inhomogeneous layers are frequent in term of porosity variations for thick layers [37]. The origin of this two peak shape in relation to the effects of anodization time, is investigated in more details in Section 4.2 and discussed in Section 5.

4.1.2 Results on p^- type sample

The same DSC experiment, performed in the same conditions for a p^- type PS sample of similar porosity (65%) and 50 μm thickness, is reported in Figure 1b. For this sample, the curve shape appears quite different than for the p^+ type: the temperature shift of the solid-liquid transition of dodecane, which shows a well defined single peak, is much larger when confined in p^- type than in p^+ type samples, reaching 32 K for freezing. This corresponds to a smaller pore radius for p^- type samples. Moreover, only a small hysteresis is observed for the confined transition of dodecane in p^- type PS, which is in agreement with our assumption related to the mechanisms involved in freezing and melting, leading to a α coefficient equals to 2 for both transitions in this case (as shown by Tab. 1).

As reported in Table 4, a pore aperture radius of 1.3 nm is estimated from the freezing curve (using formula (14) and $\alpha = 2$), whereas the melting curve (also with $\alpha = 2$) gives a pore radius of 1.5 nm in good agreement with classical gas adsorption [8] and adsorption strain [38] measurements. The peak width is 7 K for the confined

transition of dodecane in the p^- type PS layer which is a little smaller than for p^+ type PS layers, and corresponds to a narrower pore size distribution, centered around a single pore radius value.

4.1.3 First conclusions

The pore size determinations for p^- and p^+ type porous silicon are close to those obtained from isotherm adsorption measurements for similar samples. It is also worth noting that both isotherm adsorption [8] and DSC data exhibit a small hysteresis for p^- type PS samples while a larger hysteresis is clearly evidenced for p^+ type.

Therefore one can use thermoporometry to determine pore size distribution of porous silicon samples. Nevertheless, as in the case of gas adsorption method, there are some delicate points related to the interpretation of the DSC results, which will be discussed in Section 5. However, even if the absolute determination of the pore radius may be difficult, this method appears to be well suited to study the evolution of pore size distribution of p^- and p^+ type PS samples under various effects, as shown below for pure chemical dissolution or variation of anodization time.

4.2 Pore size distribution as a function of electrochemical conditions

To investigate the origin of the double peak shape of the pore size distribution observed on p^+ type PS layer, we have considered various effects which can be responsible for a broadening of the confined peak. One possible origin of this double peak shape is a porosity gradient with depth in the porous layer. Two opposite effects have been suggested in other studies [39]:

- the gradient could arise from the chemical dissolution of the porous layer already formed and immersed in HF while the bottom part of the layer is being etched. This effect may be important due to the long etching time of 700 s for the 100 μm thick p^+ type PS sample of 60% porosity;
- the gradient can also be the result of a change in the HF concentration due to diffusion problems through the porous layer, leading to a modification of the electrochemical conditions, during etching, at the bottom of long pores. This effect could then be important since the current density is high (180 mA/cm^2).

In order to study these effects, we performed several experiments, first to investigate the effect of the anodization time, and then on the consequences of etch stops during anodization. Finally, the pure chemical dissolution (without electrical current) of PS layers of p^- and p^+ type is presented and all these results are discussed.

4.2.1 Effect of anodization time

p^+ type PS samples of 60% porosity, obtained after various etching times, are compared (generally the thickness is assumed to be linearly dependent with the etching time).

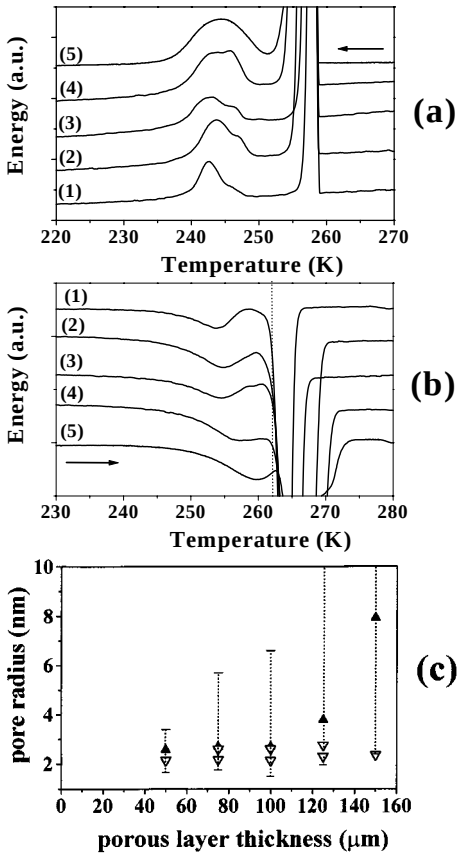

Fig. 2. (a) DSC freezing curves for dodecane confined in p^+ type PS layers of 60% porosity and of various thicknesses: (1) 50 μm, (2) 75 μm, (3) 100 μm, (4) 125 μm, (5) 150 μm. (b) DSC melting curves for the same samples. (c) The resulting pore radius plotted *versus* the sample thickness. The symbols (▲) correspond to pore radii calculated from the melting whereas the symbols (▽) correspond to pore radii calculated from the freezing DSC curves.

In Figure 2a and b, the DSC freezing and melting curves obtained for the transition of dodecane in five p^+ type PS layers of increasing thicknesses (from 50 to 150 μm) show different shapes. With the 50 μm thick PS layer, one can see the presence of a single confined freezing peak, centered at the same temperature as the most shifted confined peak of the 100 μm thick sample, corresponding to a pore radius $r = 2.1$ nm. One observes as well, a shoulder appearing for the same temperature than the second maximum of the 100 μm thick PS layer confined peak ($r \approx 2.5$ nm), whose intensity is increasing as the thickness increases. From the melting curves, one sees the confined peak position being less and less shifted as a function of sample thickness (*i.e.* of etching time) with an increase of the FWHM of the confined peak (from 7.6 K for the 50 μm thick sample to 10 K for the thicker one). We note that for the 150 μm thick PS layer the double peak shape is no more observed.

The resulting pore radii (estimated as explained in Sect. 4.1, with $\alpha = 2$ for freezing and $\alpha = 1$ for melting), are plotted *versus* sample thickness in Figure 2c.

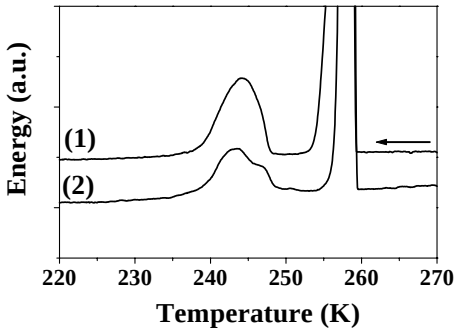

Fig. 3. DSC freezing curves of dodecane confined in two p^+ type PS layers of 60% porosity: (1) discontinuously anodized (5 steps of 140 s, each separated by a break of 15 s), (2) anodized continuously during $t = 700$ s.

The graph clearly shows an increase of the mean pore radius for heating, whereas the average size of pore aperture (for cooling) remains nearly constant for all the samples (with only a change from a single to a double peak shape). For each calculated pore radius in Figure 2c, the dotted line represents the pore size distribution width calculated from the DSC peak FWHM. For the two thicker samples this line reaches very large pore radii but it is difficult to precisely estimate them since melting confined and bulk peaks are not well separated (and the pore radius is $1/\Delta T$ dependent). The variation of the DSC peak shape will be discussed in Section 4.2.4.

4.2.2 A PS layer formed with a discontinuous etching time

In order to study the influence of the possible change in HF concentration during etching on the pore size distribution shape, we performed a formation experiment with etch stops: to form a 60% porosity PS sample of 100 μm thickness, the anodization was performed in 5 steps of 140 s, each separated by 15 s meanwhile the current density was set to zero in order to allow regeneration of the HF concentration at the pore tips. This idea, suggested a long time ago [40], was applied recently for short time breaks in the microsecond range [41], and for long time similar to that used in this work [42].

The resulting freezing DSC curve of dodecane in the etch-stop sample is plotted in Figure 3 in comparison to a "classical" p^+ type PS layer of 60% porosity and 100 μm thickness. One can notice that the two PS layers lead to different peak shapes: the etch-stop sample presents a single maximum confined peak for freezing, corresponding to a pore value of 2.2 nm, whereas the double peak of the "normal" sample corresponds to pore radii of 2.1 and 2.6 nm (see Tab. 4). The freezing peak of the etch-stop PS layer exhibits a FWHM of 6 K against 7 K for the normal one, which in term of pore size distribution width is much smaller. Therefore a discontinuous etching produces a more homogeneous porous layer in term of pore size and prevents the pore size distribution from a double peak shape.

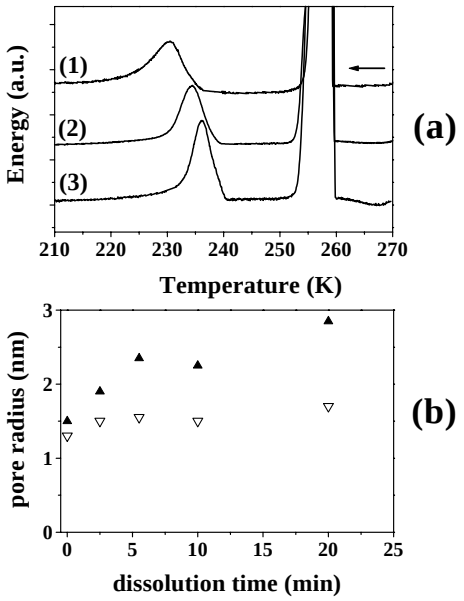

Fig. 4. (a) DSC freezing curves, showing the solid-liquid transition of dodecane confined in a p^- type PS layer of 65% porosity: (1) as formed; after a chemical dissolution of (2) 5.5 min, (3) 20 min. (b) The resulting pore radius (calculated from the temperature shift), is plotted as a function of dissolution time in a 5% HF solution. The symbols (▲) correspond to pore radii calculated from the melting whereas the symbols (▽) correspond to pore radii calculated from the freezing DSC curve.

4.2.3 Chemical dissolution

Chemical dissolution of PS samples in HF is a classical process performed for instance to increase the luminescence efficiency of PS samples [1]. The aim of the present study is to investigate the effect of such dissolution on the pore size distribution by using the DSC technique.

Pure chemical dissolution occurs when the sample is in HF solution not only in the absence of any applied voltage, but also during the electrochemical dissolution. We choose a 5% ethanoic HF concentration since the silicon dissolution rate is high [43], in order to have large effects. The chemical dissolution was performed after the PS formation, in the dark (as during the sample formation) to prevent parasitic photodissolution [44].

Chemical dissolution of p^- type PS samples

Phase transitions of dodecane confined in p^- type PS layers of 65% porosity and 50 μm thickness, have been investigated after a chemical dissolution time varying from 0 to 20 min. The experimental curves obtained for freezing, as well as the pore radius variations plotted as a function of dissolution time are presented in Figures 4a and 4b, and shows the following features:

- the maximum of the confined peak is shifted towards the bulk peak when dissolution time increases, in accordance with an increase of the average pore radius;
- the confined peak shape is modified during dissolution; the width of the confined peak decreases when the time in HF solution increases;

– in Figure 4b, the plot of pore radius *versus* dissolution time clearly shows that the difference between the melting and the freezing curve increases with dissolution time;
– for the larger dissolution time, the dependence of the pore radius *versus* etching time appears to saturate;
– if the pore radius is assumed to be linearly dependent on dissolution time (*i.e.* for short dissolution times), one can estimate a dissolution rate of 0.6 Å/min for p^- type PS layers. This value is close to p^- type bulk silicon dissolution rate in the same 5% HF ethanoic solution, measured by Halimaoui [43]: 0.5 Å/min, and only slightly different from the dissolution rate found by Hu *et al.* [45] for bulk n+(111) silicon in 48% aqueous HF: 0.3 Å/min.

Chemical dissolution of p^+ type PS samples

The same experiment was performed on p^+ type samples, using cyclohexane as the confined fluid. For cyclohexane one can study either the solid-liquid transition occurring at 279.5 K for the bulk, or the solid-solid transition (at 186 K) with a higher latent heat, giving then a more intense confined peak (see Tab. 3). DSC curves, corresponding to solid-liquid and solid-solid transition of cyclohexane for cooling, are reported in Figures 5a and 5b, for p^+ type PS samples of 100 μm thickness and an initial porosity of 60%, corresponding to various dissolution times, up to 100 min (after the formation which lasts 12 min).

As previously done, the pore radius is calculated from the temperature shift (using formula (14) and with a solid-liquid interfacial free energy [32] $\gamma_{sl} = 4.6$ mJ/m^2) and is then plotted *versus* dissolution time in Figure 5c in the range from 0 to 100 min. The following features are pointed out from Figure 5:

– as for p^- type, an increase of the mean pore radius is observed with dissolution time both from solid-solid and solid-liquid transitions. From the melting curves, one finds the mean pore radius to increase from 4 nm to more than 7 nm after 100 min in the HF solution;
– the confined peak shape is modified by chemical dissolution. Indeed, the width of the confined peak decreases (from 13 to 6 K after 100 min of dissolution): the chemical dissolution seems to happen preferentially for small pores leading to a narrower pore size distribution;
– for each dissolution time, the pore radii calculated from freezing and melting are very similar for small dissolution times (as predicted by the change in α coefficient: $\alpha = 1$ for melting and $\alpha = 2$ for freezing), but the pore aperture size seems to saturate before pore radius;
– a dissolution rate can be estimated from the experimental data to be of about 0.4 Å/min, once again close to bulk silicon dissolution rate in the same HF solution [43].

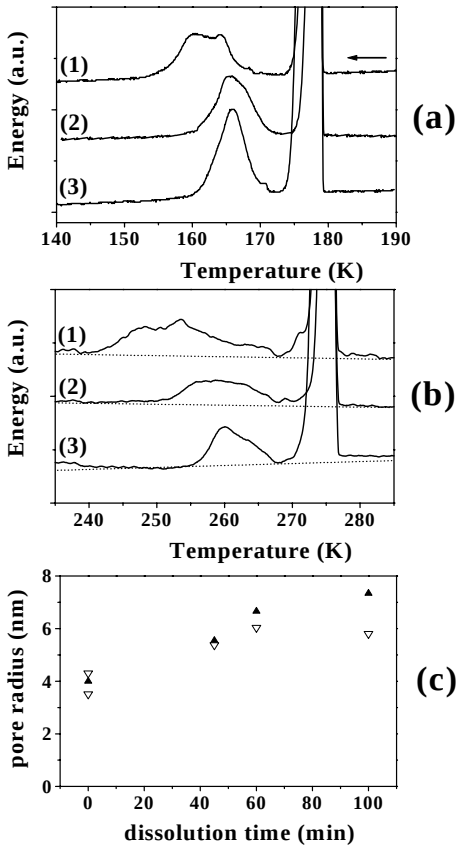

Fig. 5. DSC curves upon cooling showing (a) the solid-solid, (b) the solid-liquid phase transition of cyclohexane, confined in a p^+ type PS sample of 60% porosity: (1) as formed; after a chemical dissolution of (2) 45 min, (3) 100 min. (c) The resulting pore radius, calculated from the temperature shift of the solid-liquid transition, is plotted as a function of dissolution time in a 5% HF solution. The symbols (▲) correspond to the pore radii calculated from the melting of cyclohexane, and the symbols (▽) to the pore radii calculated from the freezing of cyclohexane.

4.2.4 Discussion

We first focus on chemical dissolution: few detailed investigations of chemical dissolution of PS layers in HF solution have been reported. From the weight measurement of PS samples *versus* the etching time in HF, Halimaoui [43] was able to follow the chemical dissolution: for short time there is a linear dependence of the mass loss *versus* time followed by a saturation, which is explained by a decrease of the specific area with etching time. However this explanation is not directly at the origin of the saturation observed by DSC since here, we get directly the average pore size and the distribution.

A possible origin of the saturation observed by DSC can be related to curvature effects since the chemical dissolution rate depends upon the radius of curvature of a crystallite. As stated in Section 2, a fluid confined in a small pore of radius r has a chemical potential (μ), different from that of the bulk liquid [13], which depends upon $1/r$. Therefore one can wonder whether a PS pore

network filled with a liquid is actually at the thermodynamical equilibrium. If this is the case, the pressure and/or HF concentration vary with the pore radius. If the system is not at equilibrium, the chemical potential is different for pores of different sizes. In both cases, the second law of thermodynamic imposes that an evolution of the system, would lead to a lower gradient of chemical potential in the whole fluid (bulk and confined). Then the chemical dissolution should be more efficient in the smallest pores. This can explain what is observed for both p^- and p^+ type material during pure chemical dissolution: for the first one the width of the confined DSC peak decreases, while for the second type, one starts with a double-peak shape which becomes after few tens of minutes in HF a narrow peak. In Figure 5, corresponding to p^+ type, the confined peak of the smallest pores (observed at lower temperature) seems to rapidly shift during dissolution to the largest ones leading to a narrower pore size distribution.

Moreover for both p^- and p^+ type, it appears that the calculated radius is different for melting and freezing (see Figs. 4b and 5c). According to the model used, freezing is sensitive to pore aperture and melting to pore size. Therefore, it appears for both p^- and p^+ type that pore aperture remains nearly constant (mainly in the case of p^- type where pore apertures are smaller), while pore size increases with dissolution time. This tendency would mean that the chemical dissolution rate is indeed a function of the curvature of silicon crystallites. However, in average, the dissolution rate in PS is nearly the same than for bulk silicon.

In the case of thick samples, the same feature is observed: the pore radius increases, while the pore aperture remains nearly constant as a function of etching time. This shows that once more, chemical dissolution occurs and, the chemical dissolution rate during anodization depends upon the radius of curvature.

However for thick PS layers, the HF concentration appears also to decrease due to diffusion problems through the pore network and lead then to non-homogeneous PS layers. A lower HF concentration, associated with the same current density, would lead to a different porosity as well as to a smaller pore size [8]. As the etch-stop PS layer exhibits only a single maximum freezing peak, one can assume that a stop of 15 s in anodization time, allowing an homogeneous HF concentration, is sufficient to lead to a single mean pore size, *i.e.* the origin of the double pore size distribution was most probably related to a change of HF concentration during anodization. Moreover, by reflectance spectroscopy, Thönissen *et al.* [39] were able to separate the effect on the porous layer structure of chemical dissolution from that of a change in HF concentration, and concluded to a dominant effect of the change in HF concentration with depth leading to a porosity gradient (at least in the chosen experimental conditions: a high current density and a 25% HF electrolyte). For both studies, the result obtained for the etch-stop PS sample, confirms the main effect of the decrease of HF concentration during etching.

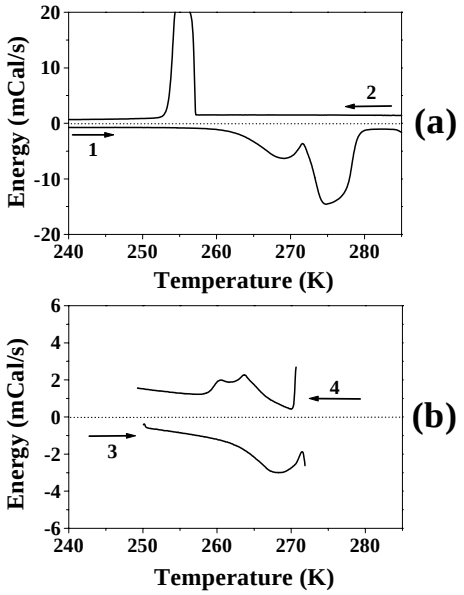

Fig. 6. DSC curves at a scanning rate of 2.5 K/min, for water confined in a thermally oxidized p^+ type PS sample of 60% porosity and 100 μm thickness: (a) a full cycle, (1) increasing and (2) decreasing temperature, (b) for a reduced cycle: (3) increasing temperature with a stop in between the two peaks, and then (4) decreasing temperature.

4.3 The case of water

The investigation of the confinement of water in the PS pore network is a complicated case but its interest is manifold. First of all, while PS is often in contact with water (during formation, anodic oxidation, electroluminescence in liquid phase, freeze drying...), the interaction between PS and water is not yet fully understood. A direct application of the present study is for instance related to the freeze drying of PS filled with water which has been recently used to avoid the cracking of highly porous silicon layers [11].

4.3.1 Results on p^+ type PS samples

After being detached, the PS layers were thermally oxidized at 300 °C under oxygen atmosphere for one hour. This oxidation allows the internal surface to become hydrophilic [30,46]. Except from this supplementary step, the experimental process was identical to the previous ones.

The result of the experiment performed on a p^+ type layers of 60% porosity and 100 μm thickness, is presented in Figure 6a, where the most surprising feature is the absence of a confined peak on the freezing DSC curve. Even after several scanning cycles, there is still only one single freezing peak. This feature can be easily explained by the large nucleation hysteresis of pure water: when the excess bulk water freezes, the nucleation delay is already more than 14 K, so it induces immediately the freezing of the confined water, giving therefore a single freezing peak

corresponding to both bulk and confined water freezing. For increasing temperature, the usual behavior is observed: the confined ice melts first, followed by the melting of bulk extended ice around 272 K.

To observe water freezing inside the pores, we had to stop the heating just after the complete melting of the confined water (*i.e.* for a temperature in between the two peaks of the melting DSC curve) [47]. Afterwards the temperature was decreased at the same constant scanning rate of 2.5 K/min, giving the DSC curves presented in Figure 6b: in such conditions, the excess bulk water does not melt, so that when the temperature is decreased, there is still a frozen bulk water crust outside the sample pore network, and the confined water freezing peak can now be observed. Figure 6b shows a double maximum for the freezing peak as usually observed for this kind of p^+ type PS sample. For freezing, the transition temperature shift is $\Delta T = 8.3$ and 4.6 K for the double freezing peak, whereas the melting curve exhibits a 3.4 K temperature shift relative to bulk melting T_0.

Nevertheless, the accurate determination of pore radius from these DSC curves appears more complicated in the case of water due to the followings points:

- in the case of water confined in nanometric sized pores, the literature reports many experimental results [29,47,48] showing the existence of a non-freezing pore water layer, with a thickness from one to three monolayers. Therefore, when considering equation (14), the estimated pore radius is underestimated due to the presence of this non-freezing layer;
- the value of $\gamma_{ice-water}$ reported in the literature [47–49] varies from 10 to 45 mJ/m^2 (with an average value around 25–30 mJ/m^2), which renders the absolute pore radius estimation difficult. But once more, if the pore radius is assumed to be the same as the one calculated from the cyclohexane DSC curves, one can estimate the value of ice-water interfacial energy. For the p^+ type PS layer of 60% porosity, the $\gamma_{ice-water}$ value is found to be 25 mJ/m^2. This is only an approximation since the non-freezing layer is neglected. However, in a first step, one can assume this layer thickness to be the same for water and alkane, and a further estimation of this non-freezing liquid layer thickness will allow us to correct the pore radius value.

At last, an important feature of this experiment is its good reproducibility, the position and intensity of the confined peak remaining the same even after several temperature cycles. This last remark means that the amount of water involved in the phase transition remains constant after the freezing of water in the pores, proving then that the porous layer does not undergo a cracking phenomenon, as we could have expected. Indeed, on the contrary to alkanes, water density is lower when frozen than when liquid. The experimental results therefore show that the water freezing induced distortions on the porous layer are not large enough to induce visible cracking effects (at least in the experimental conditions used).

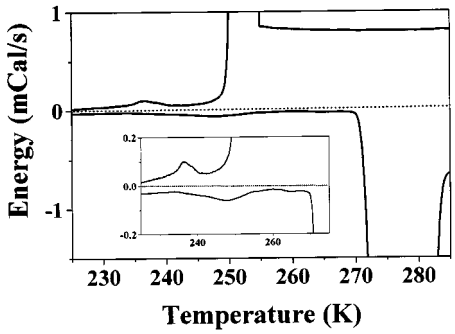

Fig. 7. DSC freezing and melting curves of water confined in a thermally oxidized p^- type PS sample of 65% porosity and 50 μm thickness, at a scanning rate of 10 K/min. A zoom of the confined peaks is shown in the insert.

4.3.2 p^- type PS layers with water

The same experiment has been performed on oxidized p^- type sample of 65% porosity and 50 μm thickness. On DSC curves plotted in Figure 7, two peaks, corresponding to bulk and confined water freezing, are clearly exhibited (even if the confined peak intensity is low due to the small amount of porous layer in this experiment). As in the p^+ case, the freezing of the external bulk water occurs at a temperature far below the bulk equilibrium melting temperature, *i.e.* with a delay of 18 K. But in the present case a confined freezing peak is present, corresponding to a temperature shift of 36 K. Moreover, a hysteresis of 10 K is observed on the confined peak larger than in the case of dodecane confined in p^- type PS samples, probably due to ice nucleation delay inside the pore network. As for p^+ type layers (and still neglecting the non-freezing layer thickness), $\gamma_{ice-water}$ can be calculated, and a value of 26 mJ/m^2 is found, close to the one calculated in the p^+ case.

4.3.3 Conclusions

The present study shows that the behavior of water confined in the PS pore network is similar to that of organic confined fluids (such as dodecane or cyclohexane). However, a special feature has to be pointed out: the nucleation delay for pure bulk water can be very large (in the 14–18 K range) inducing a single freezing peak corresponding to both bulk and confined fluid (for p^+ type samples). This last point confirms the hypothesis that freezing occurs through slow penetration of a frozen front.

As discussed in Section 5.5, freezing of water inside PS layer is an useful method to dry the sample by freeze drying [11]. However it is shown that to actually freeze water confined in p^- type pore network, one has to lower the temperature below -36 °C. Therefore precautions have to be taken in order to perform an efficient freeze drying process.

4.4 Latent heat depression of the confined fluid

In this work, we have until now neglected the possibility of a non-freezing liquid layer at the pore wall interface. It is necessary now to take into account the possible existence of this non-freezing layer in order to correct the calculated pore radius. Many experimental results on water freezing [9,29] and on organic liquids [32,33] reported a decrease in the latent heat of transition ΔH_{sl} of the confined fluid, and some of them were interpreted through the existence of a non- freezing liquid layer.

We observed a decrease of ΔH_{sl} value as a function of the decreasing pore size produced by dissolution for fluids confined in PS. The ΔH_{sl} value is estimated from the ratio of the integrated area of the confined peak by the mass of the confined liquid. This mass is the difference between the total weighted liquid mass and the bulk liquid mass estimated from the measurement of the integrated area of bulk liquid peak. The resulting confined liquid ΔH_{sl} value is found to be lowered from the bulk one by a factor 2 or 3, depending on the kind of sample considered and of the confined fluid.

This decrease in ΔH_{sl} value can be related to the excluded volume of the liquid shell surrounding the solid core. Following Lai *et al.* [50], one has:

$$\Delta H_{sl} = \Delta H_0 \left(1 - \frac{\delta V}{V}\right) \tag{15}$$

where ΔH_0 is the bulk latent heat, δV is the volume of non-freezing liquid layer and V the total volume of the pore.

For a spherical particle, one gets:

$$\delta V = \frac{4}{3}\pi \left[r^3 - (r - t_0)^3\right] \tag{16}$$

where t_0 is the thickness of the non freezing layer, and r the average pore radius.

Thus one can write for a spherical pore:

$$\Delta H_{sl} = \Delta H_0 \left(1 - \frac{t_0}{r}\right)^3 \tag{17}$$

and for a cylindrical pore:

$$\Delta H_{sl} = \Delta H_0 \left(1 - \frac{t_0}{r}\right)^2. \tag{18}$$

The confined latent heat ΔH_{sl} is estimated and then, $(\Delta H_{sl}/\Delta H_0)^{1/3}$ is plotted *versus* the inverse pore radius, $1/r$. In Figure 8a the plot corresponds to dodecane confined in p^- type samples (with spherical pores) during chemical dissolution. The bulk value of ΔH_0 (see Tab. 3) is associated with a zero value of $1/r$, since it corresponds to an infinite pore radius. The linear fit of $(\Delta H_{sl}/\Delta H_0)^{1/3}$ *versus* $1/r$, gives a t_0 value of 0.5 nm. Identically, for the cylindrical pores of p^+ type PS samples with dodecane (obtained for various etching times), $(\Delta H_{sl}/\Delta H_0)^{1/2}$ *versus* $1/r$ is plotted in Figure 8b, and the t_0 value is extracted from a linear fit. The same treatment is applied to p^- and p^+ type PS layers filled with water. One can note that the data are not accurate enough to test the exponent difference in equations (17, 18). However, we used these two equations in order to get a consistent value of t_0. All the values of non-freezing layer thickness are reported in Table 5.

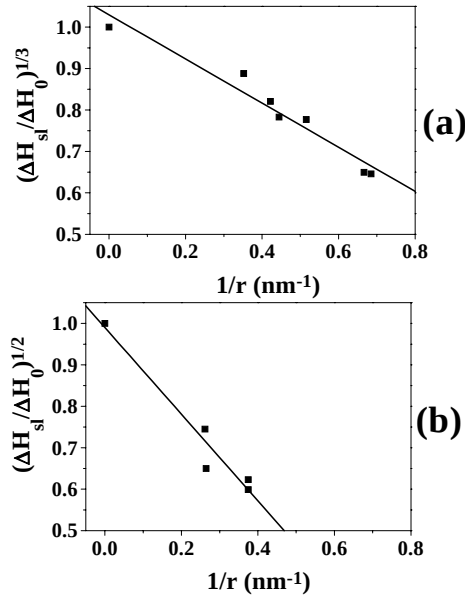

Fig. 8. Experimental data and linear fit, showing the decrease of dodecane latent heat of transition *versus* $1/r$ (where r is the pore radius): (a) for p^- type PS samples, $(\Delta H_{sl}/\Delta H_0)^{1/3}$ is plotted *versus* $1/r$ (*cf.* Eq. (17)), (b) for p^+ type PS samples, $(\Delta H_{sl}/\Delta H_0)^{1/2}$ is plotted *versus* $1/r$ (*cf.* Eq. (18)).

Table 5. Values of non-freezing layer thicknesses, t_0, for transition of dodecane and water confined in p^- and p^+ type PS, deduced from the experimental data points plotted in Figure 8.

	t_0 (nm) p^- type PS 65%	t_0 (nm) p^+ type PS 60%
with dodecane	0.5	1
with water	0.8	1.7

It is shown that the non-freezing liquid layer thickness for dodecane is larger for p^+ than for p^- type PS layers. One calculates a real pore radius of nearly 4 nm for p^+ type PS samples. This value is closer to the value estimated from isotherm adsorption measurements [8]. For p^- type, the pore radius should be then closer to 2 nm. The water non-freezing layers are thicker than organic ones, leading to larger corrections of the pore radius.

5 Discussion

In the last part, we first discuss several problems in the application of thermoporometry to the determination of pore size, in relation with our measurements on PS. Then we compare our results with results previously obtained on PS by other methods.

5.1 Validity of the thermodynamic approach

5.1.1 Free particles

For most results on the melting of small particles obtained on non-confined metallic particles, the decrease of the melting temperature can be of several hundreds K [51]. The main problem here is to choose the most relevant melting equation and to determine the best value of the surface energy.

The relation between Gibbs-Thomson equation (4) and triple point equation (6), was discussed by Kubelka [17] in 1932. He showed that these equations are equivalent if the two following conditions are satisfied:

- the particle radii are equal in the liquid and solid phase providing that the solid phase and the liquid phase have the same density. This is often a good approximation;
- the relation: $\gamma_{sv} - \gamma_{lv} = \gamma_{sl}$, which is known as Antonow relation, is satisfied [52]. This relation is obtained from Young equation in the case of perfect wetting, *i.e.* for a contact angle $\theta = 0$.

Experimentally, it is not easy to distinguish between equations (4, 6) due to the dispersion of surface energy values reported in the literature. For instance, in the case of Pb particles with $r = 25$ nm, Peppiat and Sambles [22] obtained ΔT values of 14 and 22 K using equations (4, 6) respectively. This disagreement comes from a rather large difference between their values of γ_{sv} and γ_{lv}, which do not satisfy Antonow relation.

Equation (8) for the liquid shell model is also often used for the interpretation of metal melting measurements; the thickness t_0 of the liquid shell is used as a free parameter to fit the experimental results [51]. Lai *et al.* [50] have recently used this equation for the interpretation of their nanocalorimetric measurements on the melting of Sn. As described in the reviews of Dash [28,53], the liquid shell model has received a new support with the frequent observation of surface melting on bulk samples and on small particles. Surface melting can be considered as a wetting phenomenon of the solid by its melt, which under the influence of short range interactions gives a liquid layer of a few nm thick. Lately, there was much interest in the related problem of cluster melting [54,55]. A clear discussion of this question, in relation with the thermodynamic of the liquid shell model, has been given by Reiss *et al.* [56]. The existence of surface melting for clusters of spherical [57] or cylindrical shapes [58], has been recently observed in simulations.

In addition to the choice of the melting model, another major problem for the absolute measurement of particle size is the determination of the value of γ_{sl} as measurements of solid surface are always difficult. Often γ_{sl} is determined from a measurement of the homogeneous crystallization temperature, or from the decrease of the melting temperature of small particles as indicated in the reviews of Jones [49] and Eustathopoulos [59].

5.1.2 Confined materials

In the case of confined fluids, new problems appear due to the interaction with the pore walls as well as due to the existence of disorder and defects in the crystalline structure. For thermoporometry of confined fluids, there often exists a meniscus between solid and melt, while the vapor is in equilibrium with external bulk materials. Then only the γ_{sl} term is relevant and one can use the Gibbs-Thomson equation (4). However, there appears a new parameter, the contact angle θ with the pore wall. This can lead to two opposite situations:

- the energy of the interface between the liquid and the pore wall is usually smaller than between the solid and the pore wall. This favors interface melting and the decrease of the melting temperature of the confined material. For confinement in porous silica, it is generally assumed that the wetting of the melt with the wall is perfect ($\theta = 0$), and then that the meniscus radius r is equal to the cylindrical pore radius R. However, non zero values of θ are sometimes observed, for example $\theta = 50°$ for succinonitrile in porous silica [60];
- in some cases, the wetting of the substrate by the solid phase is favored. The phenomenon of inhomogeneous nucleation in a melt by foreign solid particles is well-known. This phenomenon mainly occurs in the presence of an epitaxy between the solid material and the particle, a situation which can lead to superheating of the crystal [61].

In the case of fresh as-formed PS samples, covered by SiH_x, there is probably a perfect wetting by organic fluids [31]. On the other hand, fresh PS layers are hydrophobic [30,46], and in the case of water, it was necessary to use oxidized samples to have a good wetting. In both cases, the use of Gibbs-Thomson equation (4) is convenient, at least in a first approach.

In the case of an imperfect wetting, γ_{sl} has to be replaced by the term $\gamma_{sl} \cos\theta$ in the Gibbs-Thomson equation (4). When γ_{sl} is determined from a reference experiment on the same material, this does not modify the radius determination, as long as θ is constant, and has the same value for melting and freezing. More disturbing problems are related to two other effects, often present in phase transitions of confined fluids: the existence of a thermal hysteresis and of non-freezing layers.

5.2 Hysteresis

Our experimental curves on PS clearly show the existence of thermal hysteresis for both bulk and confined materials.

For bulk liquid, the origin of the hysteresis is well-known and is due to the delay of nucleation (probably inhomogeneous). Upon cooling it is always difficult to nucleate a crystal in the liquid. On the other hand, the nucleation of a liquid from a crystal is relatively easy as there are always defects inside and at the surface of a crystal. Originally proposed by Faraday for ice melting, and discussed in the review of Dash [28], the surface melting at a crystal surface appears to be a rather frequent phenomenon. Then, the bulk melting is expected to occur at the equilibrium bulk melting temperature, which was indeed taken as the reference temperature in our PS measurements.

For small particles, the origin of the hysteresis is related to the existence of the various definitions of melting temperatures, proposed by Peppiat and Sambles [22] and by Couchman *et al.* [24]. For measurements on confined materials, usually performed upon heating and cooling, a hysteresis is always observed although detailed discussions are rather rare.

Several mechanisms have been proposed to explain the origin of this hysteresis:

- hysteresis is classically related to nucleation delays, always present for homogeneous crystallization upon cooling. There is a general agreement that, upon heating, melting starts at the surface;
- for confined materials in contact with external unconfined materials, a specific mechanism is solid front penetration [9,26,27]. The temperature shift is due to the overcooling which corresponds to the decrease of the meniscus radius, which at equilibrium is equal to the pore size;
- another explanation for hysteresis, related to shape effects, was proposed by Brun *et al.* [9]: in Gibbs-Thomson equation (4), ΔT of the unstable equilibrium is related to curvature, which is $2/r$ for a sphere and $1/r$ for a cylinder (both with the same radius r). Brun *et al.* [9] supposed that upon heating in a cylindrical pore, a thin cylindrical liquid shell easily nucleates around a crystalline core. The melting occurs when the temperature of the cylindrical liquid shell reaches the instability condition. Then one expects a factor 2 between freezing and melting temperature shifts. Although accepted in some papers [62], this mechanism has been criticized: in a recent thermoporometry experiment, Ishikiriyama *et al.* [47] rejected this mechanism, although no other explanation was proposed for the origin of the hysteresis. They used different values of the surface energy for cooling and for heating, a strong departure from thermodynamic orthodoxy!

Here we refer the reader to a few studies dealing with materials, confined in various porous glasses, showing a nucleation related hysteresis: Aschwalom *et al.* [63] and Molz *et al.* [64] for the freezing of cryogenic fluids, and Kofman *et al.* [65] for the melting of Pb particles in a SiO or Al_2O_3 matrix. On the other hand, Grosse *et al.* [60] proposed that the hysteresis for succinonitrile is due to the dynamical contact angle hysteresis *i.e.* a change of the contact angle depending on whether the temperature is decreasing or increasing.

Our PS measurements appear to be in good agreement with the Brun *et al.* [9] model, supporting the existence of a large difference in the mechanisms for spherical and cylindrical interface shapes. We think that in this case, the shape effect gives a large contribution to the hysteresis: upon cooling the melt-solid interface is spherical, while upon heating the transition occurs when a cylindrical liquid shell becomes unstable (for p^+ type samples). On the other hand for p^- type PS layers, the hysteresis is rather small, pointing out that nucleation delays have little effect for organic liquids. One can suppose that the internal surface is rather rough, so that some liquid always remains in small crevices, reducing greatly the nucleation problem and allowing the production of a liquid layer at the interface with PS pore walls, for both the spherical shape of p^- type and the cylindrical shape of p^+ type samples.

5.3 Decrease of latent heat with size

The dependence of latent heat on the pore size has been often observed but has not been systematically studied yet. Probably, the first observations were made for ice melting. It has been known for a long time that, at a surface contact, a few monolayers of water remains liquid, reducing the apparent transition enthalpy [29].

Similar observations have been made in experiments with organic materials [9]. For instance, in experiment with cyclohexane, Mu and Malhotra [33] have observed a decrease of ΔH with size, up to 1/3 of the bulk value. The usual explanation of this ΔH reduction is related to the existence of non-freezing layers at the interface with the matrix. In very small pores, the transition enthalpy even vanishes. A similar decrease of ΔH has been observed by Unruh *et al.* [23] for indium confined in a vycor matrix. They propose a quantitative explanation where ΔH is proportional to the transition temperature, which however gives a too small effect. In nanocalorimetric measurements of tin particles, Lai *et al.* [50] also found a decrease of ΔH, in good agreement with the presence of non-freezing layer. Similar results have also been obtained for ice by Handa *et al.* [66].

5.4 Comparison between thermoporometry and adsorption measurements

In the case of adsorption and DSC experiments, the measurement methods are based on the existence of phase transitions, liquid-vapor transition as a function of pressure and solid-liquid transition as a function of temperature respectively. The thermodynamics is similar in both cases with the effect of the pressure and temperature difference related to the change of chemical potential with size.

The isotherm adsorption of gas by a porous solid occurs at low relative vapor pressures through capillary condensation, first in the smallest pores, and then in larger pores at higher vapor pressure. The low vapor pressure range enables one to determine the specific surface area of the sample by using the standard BET (Brunauer, Emmett, Teller) method [67] while the adsorption and desorption branch at higher vapor pressure give the pore size distribution [7,8].

Although more work (experimental and theoretical) has been devoted to adsorption, both methods present similar problems:

- parasitic layers: for adsorption, there is a molecular film adsorbed before the true capillary condensation, which decreases the value of the measured radius. Various empirical methods have been proposed to take into account this correction;
- hysteresis: there is also a hysteresis between increasing and decreasing pressure, which is due to the difference in the mechanisms of pore filling and emptying.

For decreasing pressure there is no nucleation problem as the meniscus propagates from the external surface of the liquid, while for increasing pressure it is necessary to nucleate some internal meniscus. Indeed, Cohan [68,69] proposed that upon decreasing pressure, the nucleation of a cylindrical meniscus inside a pore occurs at a lower pressure, since there is a ratio of 2 in the curvature between cylindrical and spherical menisci. However, this ratio is modified by the presence of the adsorbed layer. There is also a possibility of instability in the cylindrical meniscus, leading to an anticipated filling [70].

The BET method was successfully used to investigate PS layers of different doping types and levels [8]. The deduced pore size distribution of p^- and p^+ type material are almost symmetric and relatively sharp. For p^+ type, depending upon the current density (and then upon porosity), pore radius typically ranges from 2 to 11 nm, porosity being from 36 to 80%, while the specific area [8] ranges from 170 to 230 m^2/cm^3.

The pore size value for p^- and p^+ type PS samples estimated from adsorption measurements [8] and DSC are in reasonable agreement. Moreover, while a large hysteresis was clearly observed for p^+ type by both methods, only a small hysteresis was present for p^- type material. Another feature is also common for both methods: the width of the pore size distribution is larger for p^+ type samples than for p^- type samples.

Thus, in spite of the difference between the mechanisms involved in adsorption and DSC measurements (related to liquid-vapor and solid-liquid transitions respectively), the deduced results, concerning PS material, are in good agreement. It is also worth noting that DSC method can provide information about the latent heat involved in the phase transition, and is then sensitive to non- freezing layers of fluid at the interface with the matrix.

5.5 Applications to the drying of porous silicon

The luminescence properties of PS are generally efficient for high porosity material. But one of the major problems in the manufacture of PS, concerns the removal of the etchant solution which follows the PS formation [71]. A normal air-drying evaporation can lead to the cracking of highly porous materials. An increasing number of studies have been recently devoted to the drying process of PS [11,72–74]. Among them the freeze drying technique has been used [11,75]. In this drying method, the fluid inside the pore network is frozen and then sublimed under vacuum. Amato *et al.* [75] recently showed that the PS layers obtained using freeze drying, appear to have better structural and optical properties than air-dried ones. The freeze drying has the advantage of not requiring an exchange of pore media.

However, the present DSC investigation clearly shows that, to apply freeze drying efficiently on a nanoscale porous material, such as PS, the lowering of the fluid transition temperature ΔT due to the confinement has to be considered. As shown above, ΔT for water is of about 10 K for p^+ type, but can reach 36 K for p^- type! Therefore, in order to have an efficient freeze drying, the temperature should be lowered far below the usual bulk transition temperature.

6 Conclusion

This work has been devoted to the study of finite size effects on the properties of materials, confined in the small pores of PS layers. A critical review of the thermodynamical properties of small particles and confined fluids has been presented and used as a starting point in discussion of our results.

Two types (p^- and p^+) of PS materials were studied. With alkanes as the confined liquid, only a small hysteresis between melting and freezing was observed for p^- type samples with spherical pores. A larger hysteresis was clearly present for p^+ type PS samples which exhibit cylindrical pores. The existence or absence of the hysteresis is explained through different mechanisms between freezing and melting and also through the difference of pore morphology for p^- and p^+ type PS layers.

From the shift in the transition temperature of the confined material, we were able to estimate the PS layer pore size, as well as the pore size distribution width. When the non-freezing liquid layer present at the pore wall is taken into account, a pore radius of 3.7 nm is found for p^+ type, whereas p^- type PS layers exhibit a pore radius of about 2 nm. The pore size distributions have two different shapes: a narrow peak for p^- type and a double peak shape for p^+ type. Therefore, thick p^+ type PS layers are non homogeneous: this is probably due to the decrease of HF concentration during the electrochemical etching. Indeed, DSC technique appears to be suitable for the investigation of inhomogeneity in term of pore sizes of PS layers.

The effect of purely chemical dissolution has also been investigated. For the thick p^+ type layers, a double peak shape of the pore size distribution evolves towards a narrow single peak shape centered on a larger mean pore radius, showing that chemical dissolution is more efficient in the smallest pores. However in average, the rate of chemical dissolution in p^- and p^+ type PS layer (0.5 Å/min) is about the same than for bulk silicon.

Water confined in the pore network of PS material behaves in a similar way than alkanes. However it is worth noting that the temperature lowering for the confined water freezing reaches up to 36 K for p^- type. A direct application of such observations is, for instance, freeze drying of PS filled with water, which has been recently used to avoid cracking of highly porous silicon layers [11].

Finally, porous silicon exhibits a unique property among the porous material: in spite of the porosity it remains a nearly perfect single crystal. Therefore high resolution X-ray diffraction allows accurate measurement of the lattice parameter during *in situ* experiment such as vapor adsorption [38]. X-ray measurement of the strains induced by the freezing of the confined fluid are in progress in our laboratory.

We gratefully acknowledge all the scientists of the "Porous Silicon" group of our Laboratory, and in particular M. Ligeon and F. Müller, for fruitful discussions. We warmly thank V. Chamard and G. Commandeur for their help during the DSC experiments.

References

1. L.T. Canham, Appl. Phys. Lett. **57**, 1046 (1990).
2. *Porous silicon science and technology*, edited by J.C. Vial, J. Derrien (Springer, Berlin, 1994).
3. A.G. Cullis, L.T. Canham, P.D. Calcott, J. Appl. Phys. **82**, 909 (1997).
4. J. von Behren, T.V. Buuren, M. Zacharias, E.H. Chimowitz, P.M. Fauchet, Solid State Commun. **105**, 317 (1998).
5. A. Halimaoui, in *Porous silicon science and technology*, edited by J.C. Vial, J. Derrien (Springer, Berlin, 1994), p. 33.
6. M.I.J. Beale, N.G. Chew, M.J. Uren, A.G. Cullis, J.D. Benjamin, J. Appl. Phys. **46**, 86 (1985).
7. R. Hérino, in *Properties of Porous Silicon*, edited by L.T. Canham (INSPEC, The Institution of Electrical Engineers, London, 1997), p. 89.
8. R. Hérino, G. Bomchil, K. Barla, C. Bertrand, J.L. Ginoux, J. Electrochem. Soc. **134**, 1994 (1987).
9. M. Brun, A. Lallemand, J.-F. Quinson, C. Eyraud, Thermoch. Acta **21**, 59 (1977).
10. C. Faivre, D. Bellet, G. Dolino, Thin Solid Films **297**, 68 (1997).
11. G. Amato, N. Brunetto, Mater. Lett. **26**, 295 (1996).
12. R. Defay, I. Prigogine, *Tension superficielle et adsorption* (Maison Desser Editions, Liège, 1951).
13. R. Defay, I. Prigogine, A. Bellemans, D.H. Everett, *Surface tension and adsorption* (Longmans, Green & Co., London, 1966).
14. M. Brun, A. Lallemand, J.-F. Quinson, C. Eyraud, J. Chem. Phys. **70**, 979 (1973).
15. W. Thomson, Philos. Mag. **42**, 448 (1871).
16. J.J. Thomson, *Applications of dynamics to Physics and Chemistry* (MacMillan and Co., London, 1888).
17. P. Kubelka-Prag, Z. Elektrochem. **38**, 611 (1932).
18. E. Rie, Z. Physik. Chem. **104**, 354 (1923).
19. P.N. Pawlow, Chem. Abs. **3**, 860 (1909).
20. K.-J. Hanszen, Z. Phys. **157**, 523 (1960).
21. H. Reiss, I.B. Wilson, J. Coll. Sci. **3**, 551 (1948).
22. S.J. Peppiat, J.R. Sambles, Proc. R. Soc. Lond. A. **345**, 387 (1975).
23. K.M. Unruh, T.E. Huber, C.A. Huber, Phys. Rev. B **48**, 9021 (1993).
24. P.R. Couchman, W.A. Jesser, Nature **269**, 481 (1977).
25. D. Turnbull, Progr. Met. Phys. **4**, 348 (1953).
26. G.W. Scherer, J. Non-Crystal. Solids **155**, 1 (1993).
27. D.H. Everett, Trans. Faraday Soc. **57**, 1541 (1961).
28. J.G. Dash, H. Fu, J.S. Wettlaufer, Rep. Prog. Phys. **58**, 115 (1995).
29. G.K. Rennie, J. Clifford, J. Chem. Soc. Faraday Trans. 1 **73**, 680 (1977).
30. A. Halimaoui, Appl. Phys. Lett. **63**, 1264 (1993).
31. D. Bellet, G. Dolino, Phys. Rev. B **50**, 17162 (1994).
32. C.L. Jackson, G.B. McKenna, J. Chem. Phys. **93**, 9002 (1990).
33. R. Mu, V. Malhotra, Phys. Rev. B **44**, 4296 (1991).
34. G.L. Allen, R.A. Bayles, W.W. Gile, W.A. Jesser, Thin Solid Films **144**, 297 (1986).
35. M. Thönissen, S. Billat, M. Kruger, H. Luth, M.G. Berger, U. Frotscher, U. Rossow, J. Appl. Phys. **80**, 2990 (1996).
36. D.R. Uhlmann, G. Kritchevsky, R. Straff, G. Scherer, J. Chem. Phys. **62**, 4896 (1975).
37. M. Thönissen, M.G. Berger, in *Properties of Porous Silicon*, edited by L.T. Canham (INSPEC, The Institution of Electrical Engineers, London, 1997).
38. G. Dolino, D. Bellet, C. Faivre, Phys. Rev. B **54**, 17919 (1996).
39. M. Thönissen, M.G. Berger, S. Billat, R. Arens-Fischer, M. Kruger, H. Luth, W. Teiss, S. Hillbrich, P. Grosse, G. Lerondel, U. Frotscher, Thin Solid Films **297**, 92 (1997).
40. G. Bomchil, R. Herino, K. Barla, J.C. Pfister, J. Electrochem. Soc. **130**, 1611 (1983).
41. X. Hou, H. Fan, L. Xu, F. Zhang, M. Li, M. Yu, X. Wang, Appl. Phys. Lett. **68**, (1996).
42. S. Billat, M. Thonissen, R. Arens-Fischer, M.G. Berger, M. Kruger, H. Luth, Thin Solid Films **297**, 22 (1997).
43. A. Halimaoui, Surf. Sci. Lett. **306**, 550 (1994).
44. S. Létant, J.C. Vial, J. Appl. Phys. **80**, 7018 (1996).
45. S.M. Hu, D.R. Kerr, J. Electrochem. Soc. **114**, 414 (1967).
46. S. Zangooie, R. Bjorklund, H. Arwin, J. Electrochem. Soc. **144**, 4027 (1997).
47. K. Ishikiriyama, M. Todoki, K. Motomura, J. Coll. Interf. Sci. **171**, 92 (1995).
48. Y. Hirama, T. Takahashi, M. Hino, T. Sato, J. Coll. Interf. Sci. **184**, 349 (1996).
49. D.R.H. Jones, J. Mater. Sci. **9**, 1 (1974).
50. S.L. Lai, J.Y. Guo, V. Petrova, G. Ramanath, L.H. Allen, Phys. Rev. Lett. **77**, 99 (1996).
51. P. Buffat, J.-P. Borel, Phys. Rev. A **13**, 2287 (1976).
52. J.S. Rowlinson, B. Widom, *Molecular theory of capillarity* (Oxford University Press, New York, 1982).
53. J.G. Dash, Comtemp. Phys. **30**, 89 (1989).

54. R.S. Berry, Inter. J. Modern Phys. B **6**, 3695 (1992).
55. D.J. Wales, Science **271**, 925 (1996).
56. H. Reiss, P. Mirabel, R.L. Whetten, J. Chem. Phys. **92**, 7241 (1988).
57. F. Ercolessi, W. Andreoni, E. Tosatti, Phys. Rev. Lett. **66**, 911 (1991).
58. O. Gulseren, F. Ercolessi, E. Tosatti, Phys. Rev. B **51**, 7377 (1995).
59. N. Eustathopoulos, Intern. Met. Rev. **28**, 189 (1983).
60. K. Grosse, L. Ratke, B. Feuerbacher, Phys. Rev. B **55**, 2894 (1997).
61. H. Saka, Y. Nishikawa, T. Imura, Philos. Mag. A **57**, 895 (1988).
62. C. Jallut, J. Lenoir, C. Bardot, C. Eyraud, J. Membr. Sci. **68**, 271 (1992).
63. D.D. Awschalom, J. Warnock, Phys. Rev. B **35**, 6779 (1987).
64. E. Molz, A.P. Wong, M.H. Chan, J.R. Beamish, Phys. Rev. B **48**, 5741 (1993).
65. R. Kofman, P. Cheyssac, A. Aouaj, Y. Lereah, G. Deutscher, T. Ben-David, J.M. Penisson, A. Bourret, Surf. Sci. 303 (1994).
66. Y.P. Handa, M. Zakrzewski, C. Fairbridge, J. Phys. Chem. **96**, 8594 (1992).
67. S. Brunauer, P.H. Emmett, E. Teller, J. Am. Chem. Soc. **60**, 309 (1938).
68. L.H. Cohan, J. Am. Chem. Soc. **60**, 433 (1938).
69. L.H. Cohan, J. Am. Chem. Soc. **66**, 98 (1944).
70. W.F. Saam, M.W. Cole, Phys. Rev. B **11**, 1086 (1975).
71. D. Bellet, L.T. Canham, Adv. Mat. (to be published).
72. L.T. Canham, A.G. Cullis, C. Pickering, O.D. Dosser, T.I. Cox, T.P. Lynch, Nature **368**, 133 (1994).
73. O. Belmont, D. Bellet, Y. Bréchet, J. Appl. Phys. **79**, 7586 (1996).
74. J. von Behren, E.H. Chimowitz, P.M. Fauchet, Adv. Mater. **9**, 921 (1997).
75. G. Amato, N. Brunetto, A. Parisini, Thin Solid Films **297**, 73 (1997).